



SPE 159919

Extended Finite Element Modeling of Multi-scale Flow in Fractured Shale Gas Reservoirs

M. Sheng¹, SPE, G. Li, SPE, China University of Petroleum (Beijing), S.N. Shah, SPE, and X. Jin, SPE, University of Oklahoma

Copyright 2012, Society of Petroleum Engineers

This paper was prepared for presentation at the SPE Annual Technical Conference and Exhibition held in San Antonio, Texas, USA, 8-10 October 2012.

This paper was selected for presentation by an SPE program committee following review of information contained in an abstract submitted by the author(s). Contents of the paper have not been reviewed by the Society of Petroleum Engineers and are subject to correction by the author(s). The material does not necessarily reflect any position of the Society of Petroleum Engineers, its officers, or members. Electronic reproduction, distribution, or storage of any part of this paper without the written consent of the Society of Petroleum Engineers is prohibited. Permission to reproduce in print is restricted to an abstract of not more than 300 words; illustrations may not be copied. The abstract must contain conspicuous acknowledgment of SPE copyright.

Abstract

An economic production scheme for gas shale demands a better understanding of gas flow behavior and a proper reservoir simulator. The complex fracture network and multi-scale flow channel intensify the complexity of gas flow behavior. This paper integrated an improved shale-gas transport model with the extended finite element method (XFEM) to characterize the main flow mechanisms and discrete fracture network. The gas shale was viewed as the dual permeability porous media with discrete fractures. The discrete fractures are not required to be meshed, which can be placed anywhere with given location, length, and orientation. Rock deformation is implicitly coupled with gas flow to reflect stress sensitivity of gas shale. Furthermore, the displacement and matrix pore pressure across fractures are treated as discontinuous by using enrichment approximation functions. The computer coding of proposed model was developed. Terzaghi's problem for dual permeability media was considered to validate the code. The results show that pressure field is disturbed by the discrete fractures obviously, which is compared with regular pressure field obtained from the continuous fracture model. Therefore, it is important to account for discrete fractures for the fractured porous media. One case study of shale gas reservoir was presented to improve the model application. Two patterns of fracture networks were simulated in the rectangular reservoir. It is evident that the orthogonal fracture network is an ideal pattern contrast to the oblique fractures, since the former makes the pore pressure field depleted symmetrically. Furthermore, the stimulated area is the main factor to control the pressure depletion. The results confirm that the presented model and code is capable and flexible to simulate shale gas reservoir with discrete fracture network. This work provides an alternative workflow for parameter designs of hydraulic fracture and production scheme.

Introduction

Complex fracture network and multi-scale flow channels determine the complexity of gas flow behavior. A better understanding of gas transport in gas shale is significant for enhancing gas production. Until now, several flow mechanisms have been studied via experiments and modeling techniques, including the gas desorption from bulk matrix, Knudsen flow in nano-scale pores, the pressure dependence of permeability, and multi-scale flow with multiple behavior.

Recent microstructure studies showed that nanometer pores were the dominating storage zone for organics and the percentage of connected pore volume was about 60% (Curtis, 2012). Non-uniform natural fractures were observed in shale cores and outcrops with narrow width (<0.05 mm) and a main dip angle (Julia, 2008). No doubt, the combination of nano-scale matrix

¹ The visiting scholar of Prof. Subhash Shah at the University of Oklahoma.

and complexity of fracture network intensifies the challenge of modeling work. The recent modeling work primarily focuses on the interpretation of flow property of shale matrix, including gas permeability evaluation, gas adsorption, and nano flow simulation. For example, Cui et al. (2009) discussed the measurement of gas permeability and presented a new model that is explicitly correct for adsorption during pulse-decay measurements. Civan (2011) proposed a more comprehensive model, which accommodated a wide range of fundamental flow mechanisms and accounted for the non-linear term and pressure dependence of shale properties. Michel (2011) developed a unified model, which considered real gas behavior and evaluated the effect of pore size distribution on the apparent permeability. Sakhaee-Pour (2011) found that the gas permeability of shale was significantly affected by the thickness of adsorbed gas and slip flow when throat size was smaller than 50 nm. Clarkson (2012) extended the dynamic-slippage concept to shale-gas reservoirs and developed a numerical model that accounts for multimechanism flow using dynamic-slippage concept. Ambrose (2010) discussed the gas adsorption/desorption process based on the Langmuir equilibrium adsorption isotherm and using equilibrium molecular dynamics simulations. Although these studies delicately characterized many flow mechanisms in the shale matrix, they have not accounted for the interaction between matrix and fracture network.

Some researchers have begun to pay attention to this interaction effect in multi-scale. Representatively, Akkutlu (2011) introduced a new mathematical formulation for multi-scale gas transport phenomena, in which the gas flow in organic porous, inorganic porous, and fracture network was formulated. In this case, the fracture distribution is viewed as continuous, and cannot be non-uniform or discrete. The discrete fracture model (DFM) is an alternative tool for modeling shale gas reservoirs (Gong, 2011; Harikesavanallur, 2010; Weng, 2011; Lamb, 2010). Some of these authors integrated micro-seismic mappings with DFM to simulate fracture network growth and predict gas production (Harikesavanallur, 2010; Du, 2011). Rubin (2010) used fine mesh to simulate Darcy and Non-darcy flow within a stimulated reservoir volume with complex fracture network. The advantage of this approach is that it can discretely represent the geometry and orientation of real fractures. Li (2011) discussed the difference of single porosity and dual porosity model for shale gas reservoir and gave examples to demonstrate the accuracy by history match. When combining DFM with a dual porosity or permeability models, the multi-scale flow can be represented naturally. However, those DFM simulators depend on meshing technique to represent the discontinuity of fractures. The time consuming and meshing challenge will become a major problem for the high fracture density and complex connectivity case (Lamb, 2010).

Meshfree method is a kind of promising approach that do not require meshing or remeshing, eliminating the existing problems of DFM simulators. Nguyen (2008) summarized five kinds of meshfree methods in details. Out of these, the Element Free Galerkin (EFG) method and Extended Finite Element Method (XFEM) are the most popular methods used in fracture mechanics and geomechanics. They have been applied successfully in the 2D/3D arbitrary crack propagation, multi-fracture growth, and fluid flow in porous media (Bordas, 2007; Krysl, 1999; Belytschko, 1996; Mohammadnejad, 2012; Zi, 2004). However, the boundary conditions of EFG cannot be imposed as easily as XFEM, and the computational efficiency is lower than that of XFEM (Nguyen, 2008). Thus, in this study we use XFEM as our numerical tool.

XFEM was first proposed by Beytschko (1999) for modeling crack growth. This technique allows the entire crack independently of mesh to represent the discontinuous field and the near tip asymptotic field. Lamb (2010) developed a numerical scheme integrating a dual permeability model with XFEM to capture the gas flow and rock deformation in the fractured porous media. The scheme addressed the discontinuity in displacement across fractures. However, the matrix pore pressure was treated as continuous across fractures. Furthermore, the matrix was assumed as the main flow channel with Darcy order permeability. These assumptions are not appropriate for gas shale because of the nano Darcy permeability and the complexity of fracture network.

In this work, the discontinuities in pore pressure and displacement across discrete fractures were considered simultaneously. Because of the ultra-low mobility of gas in the porous matrix, the fracture network was assumed as the main flow channel. The gas flow sequence follows a certain routine: Porous matrix \rightarrow Fracture network \rightarrow Horizontal wellbore. An improved hydro-mechanical model is introduced for the fractured shale gas reservoir, which combines the dual permeability model with fracture network to capture multi-scale flow mechanisms, including mass transfer between matrix and fractures, four kinds of

flow regimes, and pressure dependence. The numerical scheme was constructed based on an enriched finite element approximation, which has no demand of meshing for fracture representation and flexibility to locate connected fractures anywhere.

Hydro-mechanical coupling

In the present model, gas shale is seen as a dual permeability porous media. The permeability of shale matrix is dependent on the pressure because of the nano-scale flow. The fracture permeability is constant assuming a fracture network with the same width and conductivity. It is believed that only connected fractures are effective contributors to the gas production. Therefore, disconnected fractures are ignored and viewed as a part of shale matrix. As shown in Figure 1, all fractures with certain connectivity are discretized in the 2D domain. The discontinuity in displacement and matrix pore pressure across fractures can be captured by using enrichment functions

This model considered the following assumptions, some of which are modified from the dual permeability model for continuous fracture.

1. The domain of interest is divided into two subdomains—nano-scale matrix and fractures. The fluid flow within each sub-domain is independent of the flow in the other sub-domain and any coupling between the fluid flow in the shale matrix and discrete fractures is controlled only via a leakage term, proposed by Barenblatt et al., 1960.
2. The matrix and fractures are represented by finite elements. The elements, split by fractures, are the fracture elements, as shown in Figure 1. The gas flow pressure in the fracture network is continuous. However, the displacement and matrix pore pressure are discontinuous across any fracture. This differs from the continuum assumption of fractures in the dual permeability model (Ghafouri and Lewis, 1996).
3. Both the boundary and body forces are carried by the shale matrix subdomain. However, the pressure boundary and flux are carried only by discrete fractures. All matrix boundaries are undrained because of nano order mobility. Therefore, the only flow routine of shale gas is from porous matrix to fracture network. This is different from Lamb's work (Lamb, 2010), where the porous matrix is the main flow channel.
4. Within nano-scale matrix, the fluid flow is coupled with the matrix deformation. This coupling is controlled by the rate of change of volumetric strain. Furthermore, any change of the grain volume is ignored. Therefore, the change of volumetric strain is equal to the change of pore volume:

$$\frac{\partial \varphi}{\partial t} = \frac{\partial \varepsilon_v}{\partial t} \quad (1)$$

5. The flowing fluid in the reservoir is only gas phase (single phase). For nano-scale matrix, the gas adsorption is isothermal, and gas density, permeability, and pore tortuosity are pressure-dependent. However, the compressibility of viscosity is ignored. For discrete fractures, the gas density is pressure-dependent, and the flow regime follows Darcy's law.

In the following, the subscripts 1 and 2 of each parameter indicate the nano-scale matrix and fracture network, respectively.

Gas transport equations for nano-scale matrix

The mass conservation of flowing gas, considering the gas adsorption and mass transfer between matrix and fractures, is given by:

$$\left[\frac{\partial (\rho \varphi)}{\partial t} + \nabla \cdot (\rho \mathbf{u}) + \frac{\partial [(1-\varphi)q]}{\partial t} \right]_1 - \rho_1 \frac{K_1}{\mu_1} (p_1 - p_2) = 0 \quad (2)$$

The Darcy's law without considering gravitation is given as:

$$\mathbf{u} = -\frac{K_1}{\mu} \nabla p \quad (3)$$

where, ρ , ϕ , \mathbf{u} , and μ denote the density, porosity, flow velocity vector, and dynamic viscosity of the flowing gas, respectively, q (kg/m^3) the mass of adsorbed gas per solid volume, K_1 the apparent permeability of shale matrix, which will be specially discussed in the Part 3. p_1 and p_2 denote the matrix pore pressure and fracture flow pressure, respectively.

Substituting Eq.1 and Eq.3 into Eq.2 and considering pressure-dependent parameters of gas density, intrinsic permeability, and tortuosity, the governing equation of gas transport in shale matrix is:

$$\left[\rho_1 \phi_1 \beta_\rho + (1 - \phi_1) K_a \rho_1 \beta_\rho \right] \frac{\partial p_1}{\partial t} + (\rho_1 - q_1) \frac{\partial \varepsilon_v}{\partial t} = \rho_1 \frac{K_1}{\mu_1} \beta_1 \left[\left(\frac{\partial p}{\partial x} \right)^2 + \left(\frac{\partial p}{\partial y} \right)^2 \right] + \rho_1 \frac{K_1}{\mu_1} \left(\frac{\partial^2 p}{\partial x^2} + \frac{\partial^2 p}{\partial y^2} \right) + \rho_1 \frac{K_1}{\mu_1} (p_1 - p_2) \quad (4)$$

where, K_a is a variable defined by Civan (2011) as

$$K_a = \frac{\rho_s M_g}{\rho \beta_\rho V_{std}} \frac{q_L p_L}{(p_L + p)^2} \quad (5)$$

$$\beta_1 = \beta_\rho + \beta_K \quad (6)$$

where, β_ρ and β_K denote the compressibility coefficients of gas density and apparent permeability. ε_v denotes the volumetric strain of solid matrix.

The mass of gas adsorbed per solid volume was estimated by means of the Langmuir isotherm, given by:

$$q = \frac{\rho_s M_g}{V_{std}} \frac{q_L p}{p_L + p} \quad (7)$$

where ρ_s denotes the material density of the measured sample, q_L Langmuir gas volume, V_{std} molar volume of gas at standard temperature (273.15K) and pressure (1atm), p gas pressure, and M_g molecular weight of gas, i.e. CH_4 .

Compared with the dual permeability model (Mao, 1994; Ghafouri and Lewis, 1996; Lewis, 1997; Lamb, 2010), no terms have been simplified for the governing equation, in which the nonlinear quadratic gradient term, the rate of fluid accumulation due to changes in density, and the gas adsorption term were kept. The detailed deviation is shown in **Appendix A**.

Gas transport equations for fracture network

The continuity equation of flowing gas including the boundary flux of fractures is given by:

$$\frac{\partial (\rho_2 \phi_2)}{\partial t} + \nabla \cdot (\rho_2 \mathbf{u}_2) + \rho_1 \frac{K_1}{\mu_1} (p_1 - p_2) - \rho_0 Q_b = 0 \quad (8)$$

where, ρ_0 denotes the density of shale gas at standard temperature (293.15K) and pressure (1atm), Q_b boundary flux of fractures, which connects with horizontal wellbore in the shale gas reservoir.

Here, the fracture strain caused by the changes of matrix strain was ignored. However, the compressibility of gas density and Darcy flow in fractures were still considered. Therefore, the gas transport equation can be deduced as follows:

$$\rho_2 \phi_2 \beta_\rho \frac{\partial p_2}{\partial t} = \left(\rho \frac{K_{2x}}{\mu} \frac{\partial^2 p}{\partial x^2} + \rho \frac{K_{2y}}{\mu} \frac{\partial^2 p}{\partial y^2} \right)_2 + \left(K_{2x} \frac{\rho}{\mu} \beta_\rho \left(\frac{\partial p}{\partial x} \right)^2 + K_{2y} \frac{\rho}{\mu} \beta_\rho \left(\frac{\partial p}{\partial y} \right)^2 \right)_2 - \rho_1 \frac{K_1}{\mu_1} (p_1 - p_2) + \rho_0 Q_w \quad (9)$$

where K_{2x} and K_{2y} denote the anisotropic permeability, one of which is aligned with fracture axis, and the other of which is perpendicular to the fracture face.

Governing equations of rock deformation

Rock deformation and gas transport in porous media was fully coupled to describe the stress-sensitivity of shale. The linear momentum balance equation without body force is written as:

$$\nabla \cdot \boldsymbol{\sigma} = 0 \quad (10)$$

where σ denotes the total stress tensor.

According to Biot's effective stress principle, the total stress tensor can be given by:

$$\sigma = \sigma_e - \alpha m p_1 \quad (11)$$

In which σ_e is the general form of the effective stress, p_1 represents the pore pressure in the nano-scale matrix, $\mathbf{m} = [1 \ 1 \ 0]^T$ in two dimensions and α is Biot's coefficient defined as $\alpha = 1 - K_t/K_s$, with K_t and K_s denoting the bulk moduli of the porous media and the solid grains, respectively.

The constitutive equation, based on the linear elasticity theory, is written in the incremental form:

$$d\sigma = \mathbf{D}(d\epsilon - d\epsilon_0) + d\sigma_0 \quad (12)$$

where, \mathbf{D} represents the constitutive matrix of the porous matrix. Throughout this paper, tension stress will be defined as positive, whereas the pore pressure is regarded as positive in compression.

Initial and boundary conditions

The initial conditions give the full displacement and pore pressure fields at time $t=0$:

$$\mathbf{u} = \mathbf{u}_0, p_1 = p_2 = p_0 \quad \text{in } \Omega \text{ and on } \Gamma$$

where, Ω is the domain of interest and Γ its boundary. The initial displacement is computed at the initial time with the in-situ stress force and no porous fluid flow.

The boundary conditions include displacement, traction, pressure, and flux on the boundary. For the shale matrix, the displacement or traction should be imposed on the domain boundary. For the fracture network, the flow pressure or flux should be imposed on those fracture nodes, which are located on the domain boundary, as shown in Figure 1.

Permeability Evaluation for Nano-scale Matrix

The shale permeability is ultralow in the order of 10^{-21} m^2 (nanoDarcy) and pressure dependent because of its nano-scale pore structure. The nano diameter of flow channels, the same scale order as molecules, leads to its flow regime to be changed from continuum flow to free-molecular flow, depending on the Knudsen number, K_n .

For the convenience of programming, we used a unified Hagen-Poiseuille-type formulation, which incorporates the suite of the continuum, slip, transition, and free-molecular flow regimes in one equation (Beskok, 1999; Civan, 2010) to evaluate the apparent gas permeability:

$$K = K_\infty f(K_n) \quad (13)$$

where, K_∞ denotes the intrinsic permeability. $f(K_n)$ is a flow condition function given as a function of the Knudsen number, the dimensionless rarefaction coefficient α , and the slip coefficient b .

$$f(K_n) = (1 + \alpha K_n) \left(1 + \frac{4K_n}{1 - bK_n} \right) \quad (14)$$

The intrinsic permeability can be measured using the pressure pulse decay (Cui, 2009). The value of dimensionless rarefaction coefficient α is determined by an empirical correlation (Civan, 2011):

$$\frac{\alpha}{\alpha_0} - 1 = \frac{A}{K_n^B} \quad A > 0, B > 0 \quad (15)$$

where A and B are empirical fitting constants. In this paper, we used $\alpha_0=1.358$, $A=0.1780$, and $B=0.4348$ (Civan, 2011).

The Knudsen number is defined as the ratio of the mean free path of molecules to a representative path (i.e. mean hydraulic radius of capillaries).

$$K_n = \frac{\lambda}{L} \quad (16)$$

The mean free path of molecules, λ is given by (Loeb 1934):

$$\lambda = \frac{\mu}{p} \sqrt{\frac{\pi R_g T}{2 M_g}} \quad (17)$$

where μ is the viscosity of the gas in Pa.s, p is the absolute gas pressure in Pa, $R_g=8314$ J/kmol/K is the universal gas constant, T is the absolute temperature in K, and M_g is the molecular mass of the gas in kg/kmol.

The mean hydraulic radius of capillaries is given by (Carman, 1956; Civan, 2007):

$$L = 2\sqrt{2\tau_h} \sqrt{\frac{K_\infty}{\phi}} \quad (18)$$

where τ_h is the tortuosity and ϕ is the porosity of the shale matrix.

During numerical simulation, the average reservoir pressure is used to estimate the matrix permeability at each time step.

Numerical Scheme using the Extended Finite Element Method (XFEM)

The extended finite element method (XFEM) is used as our numerical tool for this model, since it is the only one independent of mesh and with high computational efficiency among other meshfree methods. As shown in Figure 1, the domain is divided by fractures into three kinds of elements: the split element, tip element, and void element. The split element indicates that it is entirely cut by a fracture. The tip element represents the element with fracture tip, which is partly cut by a fracture.

XFEM introduces two local enrichment terms into the classical finite element shape function, which consists of the modified Heaviside function and Branch function. The modified Heaviside function is responsible for determining which side of a fracture faces for the interested point mathematically, which is defined by (Beytschko et al. 1999):

$$H(\mathbf{x}) = \begin{cases} +1 & \varphi(\mathbf{x}) \geq 0 \\ -1 & \varphi(\mathbf{x}) \leq 0 \end{cases} \quad (19)$$

In Eq.19, $\varphi(\mathbf{x})$ is the signed distance from the interested point to the fracture face normally. The Heaviside function represents numerically the discontinuity.

Branch functions are used to represent the near tip asymptotic fields for tip elements in linear elasticity. They are as:

$$\Psi = \left\{ \sqrt{r} \sin \frac{\theta}{2}, \sqrt{r} \cos \frac{\theta}{2}, \sqrt{r} \sin \theta \sin \frac{\theta}{2}, \sqrt{r} \sin \theta \cos \frac{\theta}{2} \right\} \quad (20)$$

where r and θ are the polar coordinates of the point \mathbf{x} in the coordinate system centered on the tip of the fracture with the x -axis aligned with the fracture direction, as shown in Figure 2. These functions give a simple numerical method to represent the stress singular near the fracture tip.

Enriched approximation functions

The displacement and pressure approximation functions are enriched by the modified Heaviside function and Branch functions. The displacement approximation function contains three terms as follows:

$$\mathbf{u}^h(\mathbf{x}) = \sum_{I \in \mathcal{N}} N_I^I(\mathbf{x}) \mathbf{u}_I + \sum_{J \in \mathcal{N}_{cr}} \mathbb{N}_u^J(\mathbf{x}) [H(\varphi(\mathbf{x})) - H(\varphi(\mathbf{x}_J))] \mathbf{a}_J + \sum_{K \in \mathcal{N}_{tip}} \mathbb{N}_u^K(\mathbf{x}) \sum_{\gamma=1}^4 [\Psi_\gamma(\mathbf{x}) - \Psi_\gamma(\mathbf{x}_K)] \mathbf{b}_{\gamma K} \quad (21)$$

The first term indicates the standard finite element approximation and represents the continuity in the whole domain. The second term represents the discontinuity of the displacement field for split nodes, and the third term denotes the near tip asymptotic displacement field for tip nodes.

In Eq.21, \mathbf{u}_I is the nodal displacement vector of all nodes. \mathcal{N} is the set of all nodes in the mesh, \mathcal{N}_{cr} is the set of nodes whose supports are cut by a fracture, and \mathcal{N}_{tip} is the set of the nodes whose supports contain a tip. \mathbf{a}_J is the nodal enriched degrees of freedom vector associated with the modified Heaviside function; and $\mathbf{b}_{\gamma K}$ are the nodal enriched degrees of freedom vector associated with branch functions. Both \mathbf{a}_J and $\mathbf{b}_{\gamma K}$ represent additional degrees of freedom associated with enriched nodes.

The matrix pressure is approximated using a weak discontinuity method (Mohammadnejad, 2012). The approximation function can be written as:

$$p^h(\mathbf{x}) = \sum_{I \in \mathcal{N}} N_p^I(\mathbf{x}) p_I + \sum_{J \in \mathcal{N}_{cr}} \mathbb{N}_p^J(\mathbf{x}) [D(\mathbf{x}) - D(\mathbf{x}_J)] \mathcal{P}_J \quad (22)$$

where \mathcal{P}_J are additional degrees of freedom for approximating the matrix pressure. $D(\mathbf{x})$ is the distance function, which is defined as the absolute value of the signed distance function.

$$D(\mathbf{x}) = |\varphi(\mathbf{x})| \quad (23)$$

Spatial and time discretization

By applying the Galerkin method and referring to formulation of consolidation problem (Lewis et al, 1998), the discrete weak forms of the governing equations can be written as:

$$\text{Porous matrix: } (\mathbf{H}_1 + \mathbf{Q}_{r1} \bar{\mathbf{P}}_1) \bar{\mathbf{P}}_1 + (\rho_1 - q_1) \mathbf{L}_1^T \frac{d\mathbf{U}_1}{dt} + \mathbf{H}' (\bar{\mathbf{P}}_1 - \bar{\mathbf{P}}_2) + \mathbf{S}_1 \frac{d\bar{\mathbf{P}}_1}{dt} = 0 \quad (24)$$

$$\text{Fracture network: } (\mathbf{H}_2 + \mathbf{Q}_{r2} \bar{\mathbf{P}}_2) \bar{\mathbf{P}}_2 - \mathbf{H}' (\bar{\mathbf{P}}_1 - \bar{\mathbf{P}}_2) + \mathbf{S}_2 \frac{d\bar{\mathbf{P}}_2}{dt} = \bar{\mathbf{f}}_2 \quad (25)$$

$$\text{Rock deformation: } \mathbf{K}_1 \frac{d\mathbf{U}_1}{dt} + \mathbf{L}_1 \frac{d\bar{\mathbf{P}}_1}{dt} = \frac{d\mathbf{f}_1}{dt} \quad (26)$$

where $\mathbf{N}, \bar{\mathbf{N}}$ are the shape functions for displacement and pressure respectively; $\mathbf{B}, \bar{\mathbf{B}}$ are the geometry matrixes for displacement and pressure respectively. The definition of the coefficient matrices, the force, and flux vectors is given as follows:

$$\mathbf{K}_1 = - \int_{\Omega_1} \mathbf{B}^T \mathbf{D}_1 \mathbf{B} d\Omega \quad (27)$$

$$\mathbf{L}_1 = - \int_{\Omega_1} \mathbf{B}^T \mathbf{m} \bar{\mathbf{N}} d\Omega \quad (28)$$

$$d\mathbf{f}_1 = - \int_{\Omega_1} \mathbf{N}^T d\mathbf{b} d\Omega - \int_{\Gamma_1} \mathbf{N}^T d\hat{\mathbf{t}} d\Gamma \quad (29)$$

$$\mathbf{H}_1 = \int_{\Omega_1} \bar{\mathbf{B}}^T \frac{\rho_1 K_1}{\mu_1} \bar{\mathbf{B}} d\Omega, \quad \mathbf{H}_2 = \int_{\Omega_2} \bar{\mathbf{B}}^T \frac{\rho_2}{\mu_2} \begin{bmatrix} K_{2,x} & 0 \\ 0 & K_{2,y} \end{bmatrix} \bar{\mathbf{B}} d\Omega \quad (30)$$

$$\mathbf{H}' = \int_{\Omega_{1,2}} \bar{\mathbf{N}}^T \frac{\rho_1 K_1}{\mu_1} \bar{\mathbf{N}} d\Omega \quad (31)$$

$$\mathbf{Q}_{r1} = \int_{\Omega_{12}} \bar{\mathbf{B}}^T \frac{\rho_1 K_1}{\mu_1} \beta_1 \mathbf{m} \bar{\mathbf{N}} d\Omega, \quad \mathbf{Q}_{r2} = \int_{\Omega_2} \bar{\mathbf{B}}^T \frac{\rho_2}{\mu_2} \beta_\rho \begin{bmatrix} K_{2x} & 0 \\ 0 & K_{2y} \end{bmatrix} \mathbf{m} \bar{\mathbf{N}} d\Omega \quad (32)$$

$$\mathbf{S}_1 = \int_{\Omega_1} \bar{\mathbf{N}}^T [\rho_1 \varphi_1 \beta_\rho + (1 - \varphi_1) K_a \rho_1 \beta_\rho] \bar{\mathbf{N}} d\Omega, \quad \mathbf{S}_2 = \int_{\Omega_2} \bar{\mathbf{N}}^T \rho_2 \varphi_2 \beta_\rho \bar{\mathbf{N}} d\Omega \quad (33)$$

$$\bar{\mathbf{f}}_2 = -\rho_0 \int_{\Gamma_2} \bar{\mathbf{N}}^T \mathbf{Q}_w d\Gamma \quad (34)$$

In Eqs. 24 and 25, the quadratic term of pressure gradient was approximated by using the last step value as follows:

$$\bar{\mathbf{P}} \cdot \bar{\mathbf{P}} = \bar{\mathbf{P}}^{t_n} \cdot \bar{\mathbf{P}}^{t_{n+1}} \quad (35)$$

The time discretization is carried out by the generalized trapezoidal method, which is an implicit method. A field function \mathbf{U} can be evaluated in the time interval $[t_n, t_{n+1}]$:

$$\mathbf{U}^{n+\alpha_t} = (1 - \alpha_t) \mathbf{U}^n + \alpha_t \mathbf{U}^{n+1} \quad (36)$$

$$\text{where } \alpha_t = \frac{t - t_n}{\Delta t_n} \quad (0 \leq \alpha_t \leq 1)$$

when α_t is equal to zero, the approximation becomes unconditionally stable without spurious rippling effects, but it has a poor accuracy and small time increment. When $\alpha_t = 2/3$, the accuracy is improved extensively, but rippling effects are possible, which can be avoided by selecting an appropriate time increment. In this paper, we found the results were accurate enough using $\alpha_t = 2/3$. Besides, t_n denotes the previous time and Δt_n denotes the incremental time step.

Integrating the spatial and time discretization schemes, the implicit matrix equation is derived as:

$$\begin{bmatrix} \mathbf{K}_1 & \mathbf{L}_1 & \mathbf{0} \\ (\rho_1 - q) \mathbf{L}_1^T & \mathbf{S}_1 + (\mathbf{H}_1 + \mathbf{Q}_{r1} \bar{\mathbf{P}}_{1,t_n} + \mathbf{H}') \Delta t_n \alpha_t & -\mathbf{H}' \Delta t_n \alpha_t \\ \mathbf{0} & -\mathbf{H}' \Delta t_n \alpha_t & \mathbf{S}_2 + (\mathbf{H}_2 + \mathbf{Q}_{r2} \bar{\mathbf{P}}_{2,t_n} + \mathbf{H}') \Delta t_n \alpha_t \end{bmatrix}_{t_n+\alpha_t} \begin{bmatrix} \bar{\mathbf{U}}_1 \\ \bar{\mathbf{P}}_1 \\ \bar{\mathbf{P}}_2 \end{bmatrix}_{t_{n+1}} = \begin{bmatrix} \mathbf{K}_1 & \mathbf{L}_1 & \mathbf{0} \\ (\rho_1 - q) \mathbf{L}_1^T & \mathbf{S}_1 - (\mathbf{H}_1 + \mathbf{Q}_{r1} \bar{\mathbf{P}}_{1,t_n} + \mathbf{H}') \Delta t_n (1 - \alpha_t) & \mathbf{H}' \Delta t_n (1 - \alpha_t) \\ \mathbf{0} & \mathbf{H}' \Delta t_n (1 - \alpha_t) & \mathbf{S}_2 - (\mathbf{H}_2 + \mathbf{Q}_{r2} \bar{\mathbf{P}}_{2,t_n} + \mathbf{H}') \Delta t_n (1 - \alpha_t) \end{bmatrix}_{t_n+\alpha_t} \begin{bmatrix} \bar{\mathbf{U}}_1 \\ \bar{\mathbf{P}}_1 \\ \bar{\mathbf{P}}_2 \end{bmatrix}_{t_n} + \Delta t_n \begin{bmatrix} \frac{d\mathbf{f}_1}{dt} \\ \mathbf{0} \\ \bar{\mathbf{f}}_2 \end{bmatrix}_{t_n+\alpha_t} \quad (37)$$

where, $\bar{\mathbf{U}}_1^{t_{n+1}}$, $\bar{\mathbf{P}}_1^{t_{n+1}}$, $\bar{\mathbf{P}}_2^{t_{n+1}}$ vectors of the displacement, matrix pore pressure, and fracture flow pressure at the current time, respectively, $d\mathbf{f}_1/dt$ vector of the incremental boundary force, $\bar{\mathbf{f}}_2$ flux vector for fractures.

Fracture representation

The level set method is commonly coupled with XFEM to locate the discontinuity interface numerically. In 2D fracture model, two orthogonal level sets, namely $\varphi(\mathbf{x})$ and $\psi(\mathbf{x})$, are needed for each fracture to describe fracture lines (Stolarska, 2001). The first one measures the signed distance normal to the fracture surface as given in Eq. 38, and the second one measures the signed distance normal to the fracture tip for an arbitrary point of interest \mathbf{x} as given in Eq.39. Specifically, the zero normal level set $\varphi(\mathbf{x})=0$ describes the containing surface for the fracture. The zero tangent level set $\psi(\mathbf{x})=0$ gives the containing plane for the fracture tip which is orthogonal to the fracture surface as shown in Figure 2.

$$\varphi(\mathbf{x}) = \text{sign}(\mathbf{n}_{\mathbf{x}_\Gamma} \cdot (\mathbf{x} - \mathbf{x}_\Gamma)) \min \|\mathbf{x} - \mathbf{x}_\Gamma\| \quad (38)$$

where \mathbf{x} is the point of interest. Γ is the fracture lines. \mathbf{x}_Γ is the point on the fracture face. $\mathbf{n}_{\mathbf{x}_\Gamma}$ is the outer normal vector.

$$\psi_i(\mathbf{x}) = (\mathbf{x} - \mathbf{x}_i) \cdot \mathbf{\hat{t}} \quad (39)$$

where $\mathbf{\hat{t}}$ is a unit vector tangent to the fracture at its tip and \mathbf{x}_i is the location of the i^{th} fracture tip.

Model Validation and Case Study

The formulation of the proposed model was developed using XFEM with 4-node quadrilateral elements. In order to verify and illustrate the capabilities of the developed code, Terzaghi's problem for dual permeability media given in References (Lamb, 2010; Lewis, 1998) was considered herein. To show the workflow of model application, one case study has been solved for predicting the depletion rate of a shale-gas reservoir.

Terzaghi's problem with discrete fractures

As shown in Figure 3, the domain is fully saturated and two interconnected fractures are modeled. One of the fractures is vertical and straight with length 8m, and the other is inclined at an angle of 45 degrees and length 4m. Except the top, other boundaries are undrained. The pore pressure on the top is equal to zero at the gauge. A uniform static force of 1000 KN/m² is applied on the top initially and maintained throughout the duration of the simulation. The initial pressure is set 1000 psi. The domain of interest is assumed homogeneous and deformed in the linearly elastic range with material properties as shown in Table 1. Specially, the fractures are assumed traction free, i.e. the contact forces are ignored.

The current model is compared with the dual permeability model for fractured continuum. The only difference between them is whether fractures are discrete or not. Here, the current model is called the 'discrete model', and the reference model the 'continuum model'.

The displacement and matrix pore pressure fields are shown in Figures 4 and 5. Obviously, the local pressure around discrete fractures is not uniform, which is compared with uniform pressure field of continuum model. Furthermore, the pressure depletion rate of discrete model at point A (Figure 3) is slower than that of the continuum model as shown in Figure 6. It is reasonable that the less fracture channel, the slower pressure declines. The results of displacement and pressure indicate the discontinuity across fractures. Therefore, more attention should be focused on discrete fractures in this problem.

Case study for a shale-gas reservoir

A shale-gas reservoir was conceptually modeled with a horizontal wellbore and the given fracture network. As shown in Figure 7, a 1000m × 500m rectangular reservoir was considered with the stimulated area $W_s \times L_s$. Orthogonal and oblique fracture networks were simulated to show the capability of representing arbitrary fracture connectivities of fractures. Except the horizontal wellbore with constant pressure, other boundaries are assumed undrained. To simulate in-situ stress conditions, the horizontal principal stress and displacement are imposed on each boundary respectively, as shown in Figure 7. The input parameters for the current model are listed in Table 2, values of which are aligned with Barnett shale in the United States. Under those conditions, the variation of gas permeability is evaluated versus reservoir pressure as shown in Figure 8, which represents reasonably the realistic shale-gas reservoirs.

The pressure depletions after three years as shown in Figure 9, illustrates two different patterns of fracture network. Since the orthogonal fracture network leads to symmetrically depleted pore pressure field with higher gas recovery. Therefore, this fracture is more effective than oblique fractures. However, the realistic fracture networks have various lengths and orientations, which have been identified by micro-seismic mapping (Fisher, 2002). The framework that has been developed is able to simulate arbitrary fracture distributions with arbitrary connectivity.

Figure 10 shows the effect of stimulated area and fracture penetration on the pressure depletion. Here, the penetration ratio is defined as the ratio between the length of stimulated zone and the distance to the reservoir boundary parallel to the wellbore, i.e. $L_s/500$. We found that the stimulated area is the major factor to effect the pressure depletion. Increasing the stimulated area will enlarge the controlled drainage area of the fracture system with faster pressure depletion, which is benefit to enhance gas recovery. For the same stimulated area, the pressure-declined curve is almost same in spite of different penetration ratios. However, the deeper fracture penetration can control the farther gas-in-place than shallower fracture penetration, as shown in Figure 11.

Discussion

Our results confirm that the presented model is capable and flexible to simulate shale gas reservoir with discrete fracture network. The effect of discrete fracture on the pressure field is significant compared with continuum fracture model. Therefore, it is necessary to model fractures in discretization for further characterization of the real reservoirs. In case study, it has been found that larger the stimulated area, faster the pressure depletion is. In addition, the pressure field of orthogonal fractures is more symmetrical than oblique fractures.

In fact, micro-seismic mapping has demonstrated that hydraulic fracture treatments create large-scale fracture networks in the Barnett shale (Fisher, 2002; Xu, 2009). Integration of microseismic mapping results with production simulators is an effective and reasonable method (Mayerhofer, 2006; Gong, 2011; Du, 2011). However, until now, all commonly used simulators simulate production by finite-difference and finite element method, and are inadequate for accurate simulation of the shale-gas reservoirs (Andrade, 2010), in which the fractures demand fine unstructured grids to be represented. Compared with previous works, the proposed method integrates the improved shale gas model with XFEM, which has two major advantages: 1) there is no demand of meshing for fracture representation and flexibility to locate connected fractures anywhere. In 2010, Lamb did similar work using XFEM for fractured media. Certainly, the differences between the proposed model and Lamb's work are the pore pressure is treated discontinuously and the boundary condition of flux is imposed for fractures in this paper. 2) the proposed model accounts for many elaborated factors for accurate simulation, including discretization of fractures, dual permeability, gas adsorption effect, stress sensitivity, pressure dependence and the main flow mechanisms of shale gas. Besides, the proposed model can handle the pressure transient process using fine grids.

The results of case study indicate that the stimulated area is the primary factor to influence drainage area. For the same stimulated area, the deeper fracture penetration is proper to drain the far zone from wellbore. Therefore, the larger stimulated area is required for the shale gas production. To reach the reservoir boundary and the deeper gas-in-place, the high fracture penetration is better for the same stimulated area. To obtain a symmetrical pressure field, the orientation of natural fractures and in-situ stress should be evaluated by logging and outcrop study first. Then, the orientation of horizontal lateral can be optimized.

This work includes the traction on the fracture face is free and the fracture width is constant. Our future research will impose the fluid pressure on the fracture face and consider time dependence of fracture width. The proposed formulation can also be used for multi-phase flow problem through modeling gas and water flow in matrix and fractures separately.

Conclusions

In this paper, an improved shale gas transport model and numerical scheme based on XFEM are developed to simulate the multi-scale gas flow in the discrete fractured domain. The Knudsen flow of nano-scale matrix and Darcy flow of fractures are integrated to reflect the multi-scale flow. The effect of discrete fractures on pressure field is obvious compared with continuum fracture model. The results of case study confirmed that the developed model is applicable for the complex fracture network with different connectivities. It has been found that the orthogonal fractures are proper for shale gas production because of their symmetrical pressure field. Furthermore, the stimulated area determines the drainage area. For the same stimulated area, the deeper fracture penetration can produce the farther gas-in-place. This work shows the potential to be the next generation simulator for shale-gas reservoir.

Acknowledgements

The authors would like to thank Dr. Stéphane Borads of Cardiff University, Dr. Anthony Lamb of Imperial College London, Dr. Faruk Civan, and Dr. Deepak Devegowda of the University of Oklahoma for their valuable input. Mao Sheng would like to thank China Scholarship Council for supporting his Joint Advisory PhD Program, and also would like to thank the Well Construction Technology Center of the University of Oklahoma for providing him an opportunity to work as a visiting scholar.

References

Akkutlu, I.Y. and Fathi, E., 2011. Multi-scale gas transport in shales with local kerogen heterogeneities. Paper SPE 146422 presented at the SPE Annual Technical Conference and Exhibition, Denver, Colorado, 30 October- 2 November.

- Ambrose, R.J., Hartman, R.C., Diaz-Campos, M., et al. 2010. New pore-scale considerations for shale gas in place calculations. Paper SPE 131772 presented at the SPE Unconventional Gas Conference, Pittsburgh, Pennsylvania, 23-25 February.
- Andrade, J., Civan, F., Devegowda, D., et al. 2010. Accurate Simulation of Shale-Gas Reservoirs. Paper SPE 135564-MS presented at the SPE Annual Technical Conference and Exhibition, Florence, Italy, 19-22 September.
- Andrade, J., Civan, F., Devegowda, D., et al. 2011. Design and Examination of Requirements for a Rigorous Shale-Gas Reservoir Simulator Compared to Current Shale-Gas Simulator. Paper SPE 144401 presented at North American Unconventional Gas Conference and Exhibition, Woodlands, Texas, 14-16 June.
- Harikesavanallur, A., Deimbacher, F., Crick, M., et al. 2010. Volumetric Fracture Modeling Approach (VFMA): Incorporating Microseismic Data in the Simulation of Shale Gas Reservoirs. Paper SPE presented at the SPE Annual Technical Conference and Exhibition, Florence, Italy, 19-22 September.
- Bai, M., Ma, Q.G., and Roegiers, J., 1994. A nonlinear dual-porosity model. *Appl. Math. Modelling*. 18: 602-610.
- Barenblatt, G. I., Zheltov, I. P., and Kochina, I. N., 1960. Basic concepts in the theory of seepage of homogeneous liquids in fissured rocks. *Journal of Applied Mathematics and Mechanics* 24 (5): 1286-1303.
- Beskok, A. and Karniadakis, G.E., 1999. A model for flows in channels, pipes, and ducts at micro and nano scales. *Microscale Thermophysics Eng.* 3 (1):43-77.
- Belytschko, T and Tabbara, M., 1996. Dynamic Fracture Using Element-Free Galerkin Methods. *International Journal for Numerical Methods in Engineering* 39: 923-938.
- Bordas, S., Rabczuk, T., and Zi, G., 2007. Three-dimensional crack initiation, propagation, branching and junction in non-linear materials by an extended meshfree method without asymptotic enrichment. *Engineering Fracture Mechanics* 75: 943-960.
- Carman, P.C., 1956. Flow of gases through porous media. London: Butterworths.
- Civan, F., 2007. Reservoir Formation damage— fundamentals, modeling, assessment, and mitigation. pp. 1114, Second edition, Burlington: Gulf Professional Publishing, Elsevier.
- Civan, F., 2010. Effective correlation of apparent gas permeability in tight porous media. *Transp. Porous Med.* 82 (2): 375-384.
- Civan, F., Rai, C.S., and Sondergeld, C.H., 2011. Shale-Gas Permeability and Diffusivity Inferred by Improved Formulation of Relevant Retention and Transport Mechanisms. *Transp Porous Med* 86: 925–944.
- Clarkson, C.R., Nobakht, M., Kaviani, D., et al. 2012. Production Analysis of Tight-Gas and Shale-Gas Reservoirs Using the Dynamic-Slippage Concept. *SPE Journal*, 17: 230-242.
- Cui, X., Bustin, A.M.M., and Bustin, R.M., 2009. Measurements of gas permeability and diffusivity of tight reservoir rocks: different approaches and their applications. *Geofluids* 9: 208-223.
- Curtis, M E., Sondergeld, C.H., Ambrose, R.J., et al. 2012. Microstructural investigation of gas shales in two and three dimensions using nanometer-scale resolution imaging. *AAPG Bulletin* 96(4): 665-677.
- Du, C.M., Zhan, L., Li, J., et al. 2011. Generalization of Dual-Porosity-System Representation and Reservoir Simulation of Hydraulic Fracturing-Stimulated Shale Gas Reservoirs. Paper SPE 146534 presented at the SPE Annual Technical Conference and Exhibition, Denver, Colorado, 30 October- 2 November.
- Fisher, M.K., Davidson, B.M., Goodwin, A.K., et al. 2002. Integrating Fracture Mapping Technologies to Optimize Stimulations in the Barnett Shale. Paper SPE 77411 presented at the SPE Annual Technical Conference and Exhibition, San Antonio, Texas, 29 September-2 October.
- Ghafouri, H.R. and Lewis, R.W., 1996. A finite element double porosity model for heterogeneous deformable porous media. *Int. J. Numer. Anal. Meth. Geomech* 20: 831-844.
- Gong, B., Qin, G., Towler, B.F., et al. 2011. Discrete Modeling of Natural and Hydraulic Fractures in Shale-Gas Reservoirs. Paper SPE 146842 presented at the SPE Annual Technical Conference and Exhibition, Denver, Colorado, 30 October- 2 November.
- Julia, F.W. and Gale, J.H. 2008. Natural fractures in the Barnett Shale: constraints on spatial organization and tensile strength with implications for hydraulic fracture treatment in shale-gas reservoirs. Paper ARMA presented at the 42nd U.S. Rock Mechanics Symposium (USRMS), San Francisco, June 29 - July 2.
- Kang, S.M., Fathi, E., Ambrose, R.J., et al. 2010. Carbon dioxide storage capacity of organic-rich shales. Paper SPE 134583 presented at the SPE Annual Technical Conference and Exhibition, Florence, Italy, 19-22 September.
- Krysl P. and Belytschko, T., 1999. The Element Free Galerkin Method for Dynamic Propagation of Arbitrary 3-D Cracks. *International Journal for Numerical Methods in Engineering* 44 (6): 767-800.

- Korsawe, J., Starke, G., Wang, W.Q., et al. 2005. Finite element analysis of poro-elastic consolidation in porous media: standard and mixed approaches. *Comput. Methods Appl. Mech. Engrg.* 195: 1096-1115.
- Lamb, A.R., Gorman, G.J., Gosselin, O.R., et al. 2010. Finite element coupled deformation and fluid flow in the fractured porous media. Paper SPE 131725 presented at the SPE EUROPEC/EAGE Annual conference and Exhibition, Barcelonan, Spain, 14-17 June.
- Lewis, R.W. and Ghafouri, H.R., 1997. A novel finite element double porosity model for multiphase flow through deformable fractured porous media. *Int. J. Numer. Anal. Meth. Geomech.* 21: 789-816.
- Lewis, R.W. 1998. The finite element method in the static and dynamic deformation and consolidation of porous media. New York: John Wiley & Sons.
- Li, J., Du, C.M., and Zhang, X. 2011. Critical Evaluations of Shale Gas Reservoir Simulation Approaches: Single Porosity and Dual Porosity Modeling. Paper SPE141756 presented at the SPE Middle East Unconventional Gas Conference and Exhibition, Muscat, Oman, 31 January-2 February 2011.
- Loeb, L.B., 1934. The kinetic theory of gases. Second edition. New York: McGraw-Hill Co. Inc.
- Mayerhofer, M.J., Lolon, E.P., Youngblood, J.E., et al. 2006. Integration of Microseismic-Fracture-Mapping Results With Numerical Fracture Network Production Modeling in the Barnett Shale. Paper SPE 102103 presented at the SPE Annual Technical Conference and Exhibition, San Antonio, Texas, 24-27 September.
- Michel, G.G., Sigal, R.F., Civan, F., et al. 2011. Parametric Investigation of Shale Gas Production Considering Nano-Scale Pore Size Distribution, Formation Factor, and Non-Darcy Flow Mechanisms. Paper SPE 147438 presented at the SPE Annual Technical Conference and Exhibition, Denver, Colorado, 30 October- 2 November.
- Mohammadnejad, T. and Khoei, A.R., 2012. Hydro-mechanical modeling of cohesive crack propagation in multiphase porous media using the extended finite element method. *Int. J. Numer. Anal. Meth. Geomech.* DOI: <http://10.1002/nag.2079>.
- Moes, N., Dolbow, J., and Belytschko, T., 1999. A finite element method for crack growth without remeshing. *Int. J. Numer. Meth. Engng.* 46: 131-150.
- Nguyena, V.P., Rabczukb,T., Bordasc, S., et al. 2008. Meshless methods: A review and computer implementation aspects. *Mathematics and Computers in Simulation* 79 (3): 763-831.
- Rubin B. 2010. Accurate Simulation of Non Darcy Flow in Stimulated Fractured Shale Reservoirs. Paper SPE 132093 presented at the SPE Western Regional Meeting, Anaheim, California, USA, 27-29 May 2010.
- Sakhaee-Pour, A. and Bryant, S.L., 2011. Gas permeability of shale. Paper SPE 146944 presented at the SPE Annual Technical Conference and Exhibition, Denver, Colorado, 30 October- 2 November.
- Stolarska, M., Chopp, D.L., Moes, N. et al. 2001. Modelling crack growth by level sets in the extended finite element method. *International Journal for Numerical Methods in Engineering* 51:943-960.
- Warpinski, N.R., Mayerhofer, M.J., Vincent, M.C., et al. 2008. Stimulating Unconventional Reservoirs: Maximizing Network Growth While Optimizing Fracture Conductivity. Paper SPE 114173 presented at SPE Unconventional Reservoirs Conference, Keystone, Colorado, 10-12 February.
- Weng, X., Kresse, O., Cohen, C., et al. 2011. Modeling of Hydraulic-Fracture-Network Propagation in a Naturally Fractured Formation. *SPE Production & Operations* 26(4): 368-380.
- Xu, W., Calvez, J.L., and Thiercelin, M., 2009. Characterization of Hydraulically-Induced Fracture Network Using Treatment and Microseismic Data in a Tight-Gas Sand Formation: A Geomechanical Approach. Paper SPE 125237-MS presented at the SPE Tight Gas Completions Conference, San Antonio, Texas, 15-17 June.
- Zi, G., Song, J., Budyn, E., et al. 2004. A method for growing multiple cracks without remeshing and its application to fatigue crack growth. *Modelling Simul. Mater. Sci. Eng.* 12: 901-915.

Appendix A: Gas transport governing equation for nano-scale matrix

This derivation begins with the mass conservation for matrix and Darcy's flow, which are given as:

$$\left[\frac{\partial(\rho\varphi)}{\partial t} + \nabla \cdot (\rho \mathbf{u}) + \frac{\partial[(1-\varphi)q]}{\partial t} \right]_1 - \rho_1 \frac{K_1}{\mu_1} (p_1 - p_2) = 0 \quad (\text{A1})$$

$$\mathbf{u}_1 = -\frac{1}{\mu_1} K_1 \cdot \nabla p_1 \quad (\text{A2})$$

In which, ρ , φ , \mathbf{u} , and μ denote the density, porosity, flow velocity vector, and dynamic viscosity of the flowing gas, respectively. q (kg/m³) denotes the mass of adsorbed gas per solid volume. K_1 denotes the apparent permeability of shale matrix. p_1 and p_2 denote the matrix pore pressure and fracture pressure, respectively.

Accounting for the pressure dependence, the isothermal coefficients of compressibility for gas density, porosity, and permeability are defined as:

$$\beta_\rho = \frac{1}{\rho} \frac{\partial \rho}{\partial p} \quad (\text{A3})$$

$$\beta_K = \frac{1}{K} \frac{\partial K}{\partial p} \quad (\text{A4})$$

$$\beta_\varphi = \frac{1}{\varphi} \frac{\partial \varphi}{\partial p} = \frac{1}{K_t} = \frac{3(1-2\nu)}{E} \quad (\text{A5})$$

$$\beta_{\tau_h} = \frac{1}{\tau_h} \frac{\partial \tau_h}{\partial p} \quad (\text{A6})$$

where β_ρ , β_K , β_φ , β_{τ_h} are the coefficients of compressibility for gas density, apparent permeability, porosity, and tortuosity, respectively. K_t is the volumetric strain. E and ν are the Young's modulus and Poisson's ratio of matrix, respectively. The compressibility of porosity is derived from Assumption 4 of the model. Here, all coefficients of compressibility are assumed constant.

The following coefficient can be derived based on above individual compressibility coefficients, which is conveniently included in the governing equation.

$$\begin{aligned} \beta_1(p) &= \left(\frac{\rho}{\mu} K \right)^{-1} \frac{\partial \left(\frac{\rho}{\mu} K \right)}{\partial p} = \left(\frac{\rho}{\mu} K \right)^{-1} \left[\frac{1}{\mu} K \frac{\partial \rho}{\partial p} + \frac{\rho}{\mu} \frac{\partial K}{\partial p} - \frac{\rho}{\mu^2} K \frac{\partial \mu}{\partial p} \right] \\ &= \beta_\rho(p) + \beta_K(p) \end{aligned} \quad (\text{A7})$$

In fact, the compressibility of apparent permeability is determined by the intrinsic permeability and a function of Knudsen number, which is given as (Civan, 2011):

$$\beta_K = \beta_{K_\infty} + \beta_f \quad (\text{A8})$$

where,

$$\beta_{K_\infty} = \frac{1}{K_\infty} \frac{\partial K_\infty}{\partial p}$$

(A9)

$$\beta_f = \frac{1}{f(K_n)} \frac{\partial f(K_n)}{\partial p} = \frac{1}{f(K_n)} \frac{df(K_n)}{d(K_n)} \frac{\partial(K_n)}{\partial p}$$

(A10)

in which,

$$\frac{df(K_n)}{d(K_n)} = \alpha \left(1 + \frac{AB}{K_n^{B+1}} \right) \left(1 - \frac{4K_n}{1-bK_n} \right) + 4 \left(\frac{1+\alpha K_n}{1-bK_n} \right) \quad (\text{A11})$$

$$\begin{aligned} \frac{\partial(K_n)}{\partial p} &= \frac{\partial}{\partial p} \left(\frac{\mu}{4p} \sqrt{\frac{\pi R_g T \varphi}{M_g \tau_h K_\infty}} \right) = \frac{\mu}{4} \sqrt{\frac{\pi R_g T \varphi}{M_g}} \frac{\partial}{\partial p} \left(\frac{1}{p} \sqrt{\frac{1}{\tau_h K_\infty}} \right) \\ &= - \left(\frac{1}{p} + \frac{1}{2} \beta_{\tau_h} + \frac{1}{2} \beta_{K_\infty} \right) K_n + \frac{1}{2} \beta_\varphi K_n \end{aligned} \quad (\text{A12})$$

Eq. A2-A11 substituting into Eq. A1 can be arranged as:

$$(1) \quad \frac{\partial(\rho \varphi)}{\partial t} = \varphi \frac{\partial \rho}{\partial t} + \rho \frac{\partial \varphi}{\partial t} = \rho \varphi \frac{1}{\rho} \frac{\partial \rho}{\partial p} \frac{\partial p}{\partial t} + \rho \frac{\partial \varepsilon_V}{\partial t} = \rho \varphi \beta_\rho \frac{\partial p}{\partial t} + \rho \frac{\partial \varepsilon_V}{\partial t} \quad (\text{A13})$$

$$(2) \quad \frac{\partial[(1-\varphi)q]}{\partial t} = (1-\varphi) \frac{\partial q}{\partial t} - q \frac{\partial \varphi}{\partial t} = \rho(1-\varphi) \frac{\partial q}{\partial \rho} \frac{1}{\rho} \frac{\partial \rho}{\partial p} \frac{\partial p}{\partial t} - q \frac{\partial \varepsilon}{\partial t} \quad (\text{A14})$$

$$\begin{aligned} (3) \quad \nabla \cdot (\rho \mathbf{u}) &= - \left[\frac{\partial}{\partial x} \left(\rho \frac{K}{\mu} \frac{\partial p}{\partial x} \right) + \frac{\partial}{\partial y} \left(\rho \frac{K}{\mu} \frac{\partial p}{\partial y} \right) \right] = - \left[\nabla \left(\rho \frac{K}{\mu} \right) \cdot \nabla p + \rho \frac{K}{\mu} \nabla^2 p \right] \\ &= - \left\{ \rho \frac{K}{\mu} \beta_1 \left[\left(\frac{\partial p}{\partial x} \right)^2 + \left(\frac{\partial p}{\partial y} \right)^2 \right] + \rho \frac{K}{\mu} \left(\frac{\partial^2 p}{\partial x^2} + \frac{\partial^2 p}{\partial y^2} \right) \right\} \end{aligned} \quad (\text{A15})$$

Substituting Eq. A13-A15 into Eq. A1, and upon rearrangement the gas transport governing equation for matrix can be obtained:

$$\left[\rho_1 \varphi_1 \beta_\rho + (1-\varphi_1) K_a \rho_1 \beta_\rho \right] \frac{\partial p_1}{\partial t} + (\rho_1 - q_1) \frac{\partial \varepsilon_V}{\partial t} = \rho_1 \frac{K_1}{\mu_1} \beta_1 \left[\left(\frac{\partial p}{\partial x} \right)^2 + \left(\frac{\partial p}{\partial y} \right)^2 \right]_1 + \rho_1 \frac{K_1}{\mu_1} \left(\frac{\partial^2 p}{\partial x^2} + \frac{\partial^2 p}{\partial y^2} \right)_1 + \rho_1 \frac{K_1}{\mu_1} (p_1 - p_2) \quad (\text{A16})$$

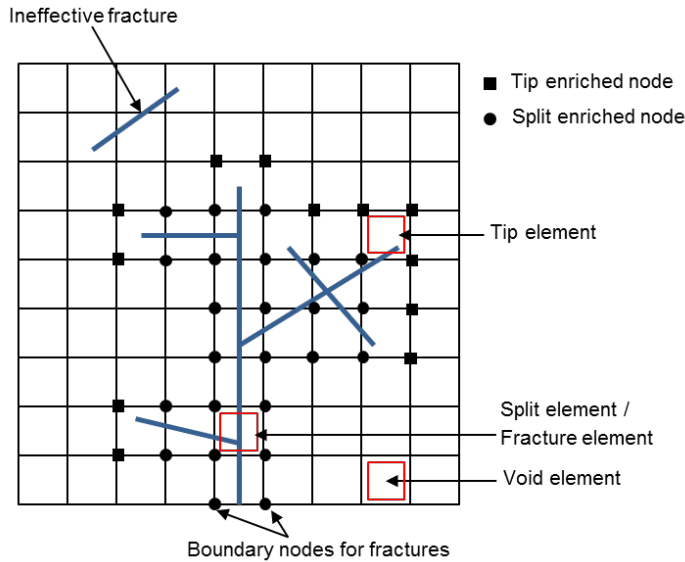
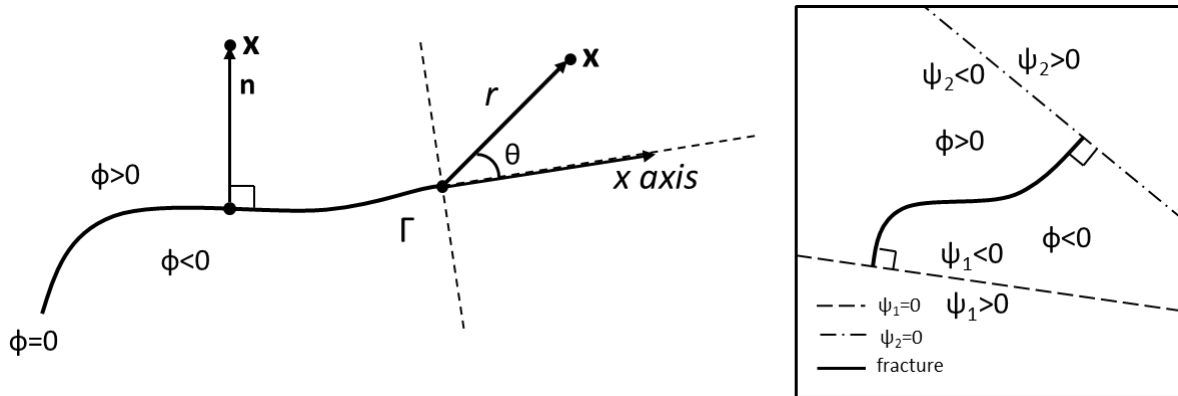


Figure 1: Schematic of discrete fracture domain with interconnected fractures and ineffective fracture. In XFEM, the types of element consist of tip element, split element and void element. In this model, the elements, split by any fracture, are viewed as the fracture element for pore pressure approximation (after Lamb, 2010). The two types of nodes representing fractures are tip-enriched nodes and split enriched node. The flux or pressure boundary is imposed on the boundary nodes for fractures.



(a) The local polar coordinates for fracture tip. r is the distance from fracture tip to the interested point x . (b) fracture description defined by level set functions. The zero normal level set $\phi(x) = 0$ describes the surface containing the crack and the zero tangent level set $\psi(x) = 0$ gives the plane containing the fracture tip.

Figure 2: The representation of fractures by level set method (after Lamb, 2010)

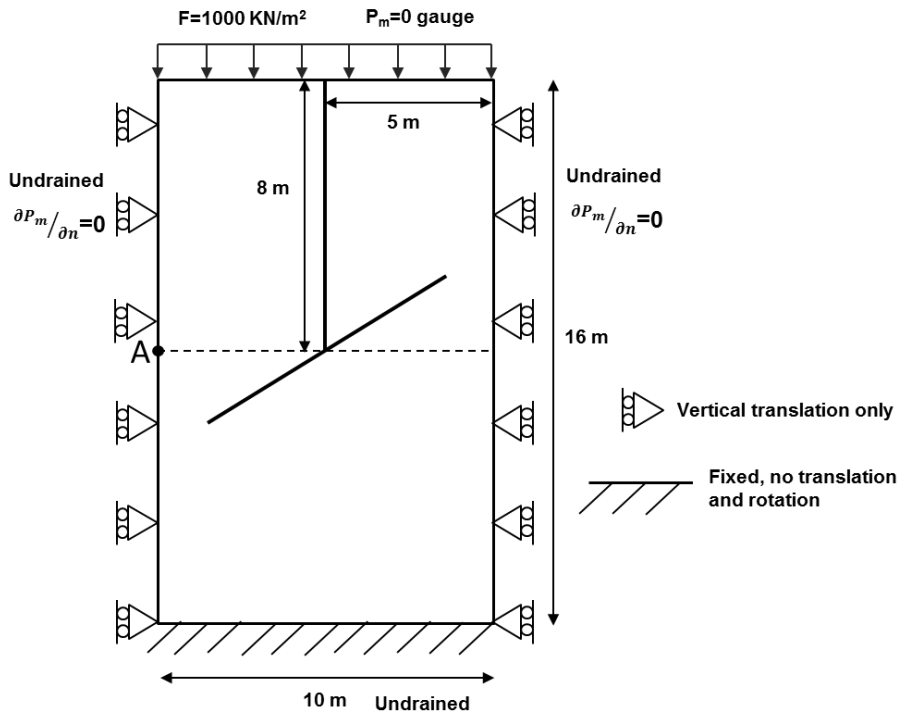


Figure 3: One dimensional Terzaghi problem; two 2D fractures were set in domain, in which the vertical fracture was connected with the inclined fracture of 45 degree; assigned boundary conditions has been shown in the diagram. A uniform static force of 1000 KN/m² is loaded on the top and the initial pressure is 1000 psi.

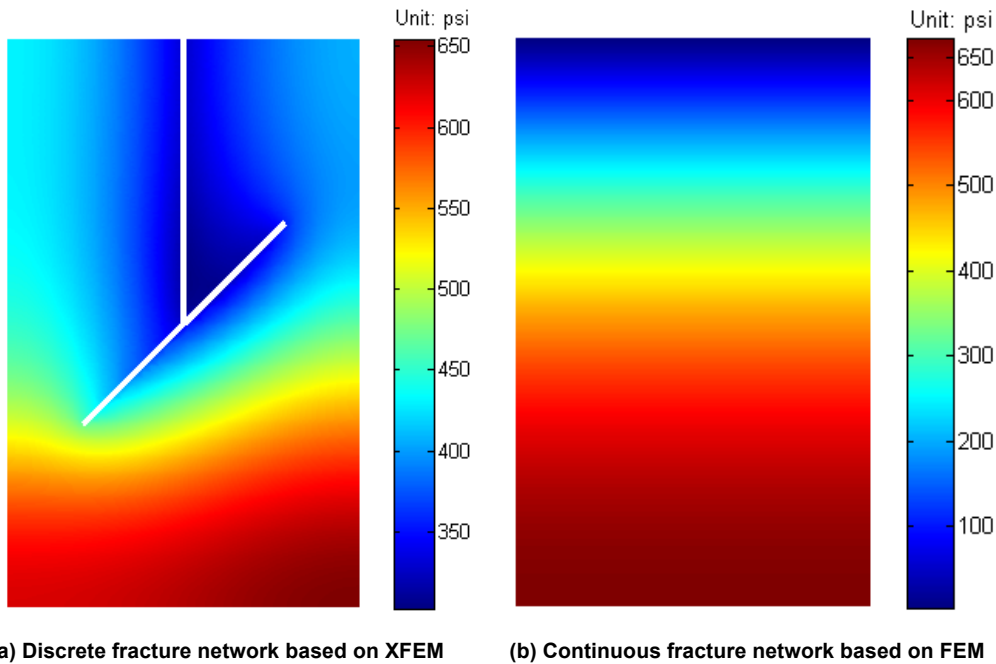


Figure 4: Matrix pore pressure distribution at the 100th day for Terzaghi's problem. The discrete fractures disturb the pore pressure field. The pore pressure is discontinuous across fractures in Figure 2(a), which is attributed to the enriched pressure function used in this paper. However, if fractures are assumed continuous, it is not able to reflect the influence of fracture geometry on the pore pressure field.

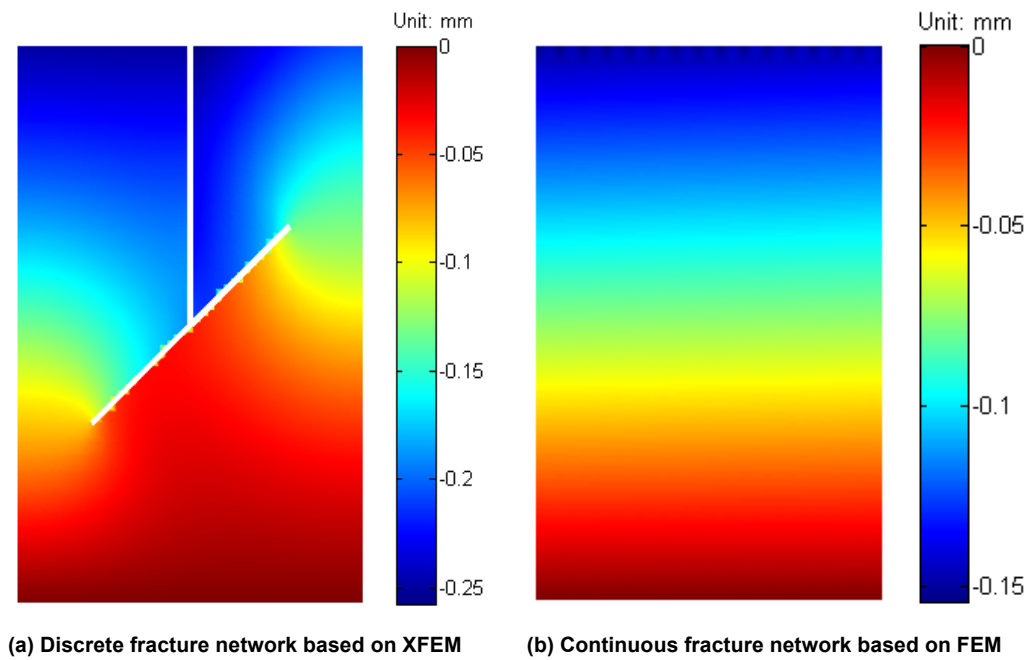


Figure 5: Displacement in Y direction, (Negative value represents down vertically). Because of discrete fractures, the displacement is discontinuity across the fractures as shown in Figure 5(a). However, the discontinuity is not considered for continuous model in Figure 5(b).

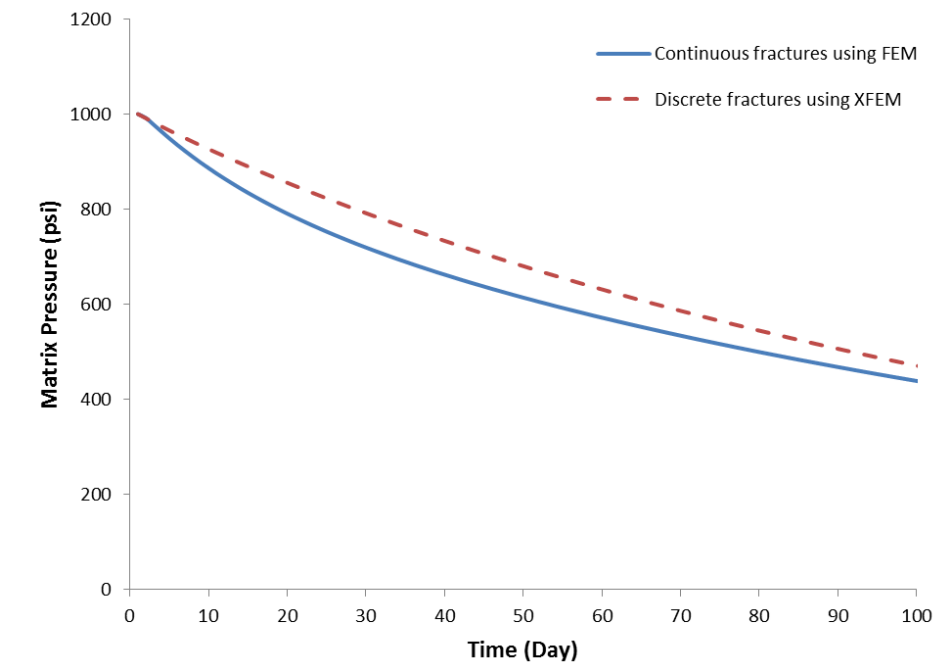


Figure 6: Matrix pore pressure versus time at point A (as shown in Figure 3).

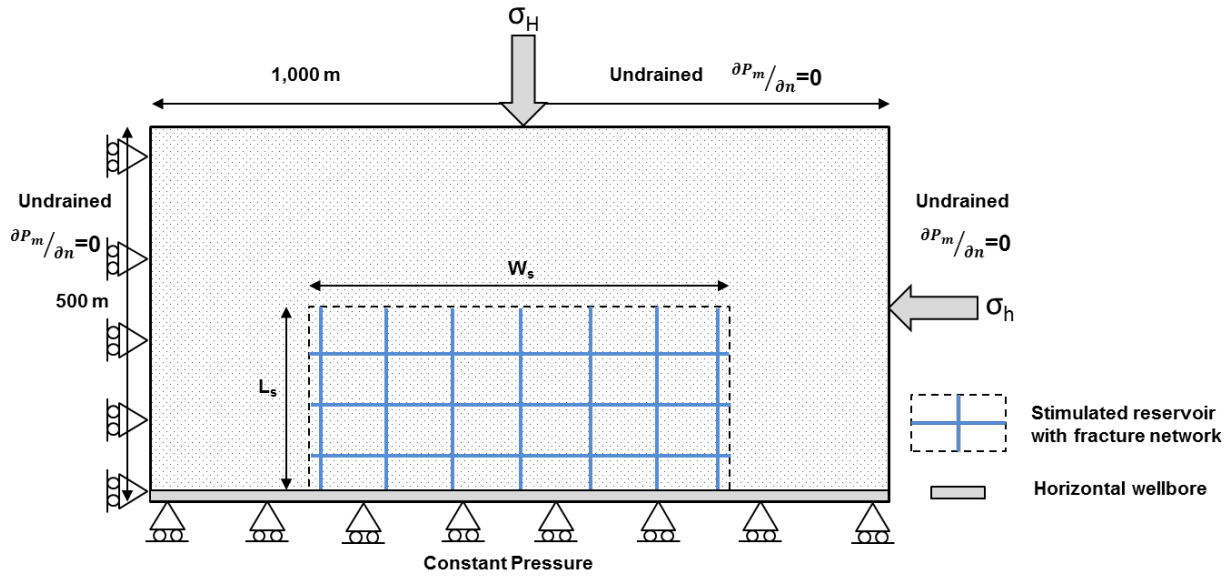


Figure 7: A rectangular-shaped shale gas reservoir with a uniform thickness. A horizontal well is across this reservoir with the length 1000m. Multistage horizontal fracturing job was conducted to form the fracture network zone. In the model, it is assumed that the only produced gas routine is from porous matrix to fracture network and into wellbore. Half of the domain was simulated with undrained boundaries. In this paper, in-situ stress is imposed as shown in this figure.

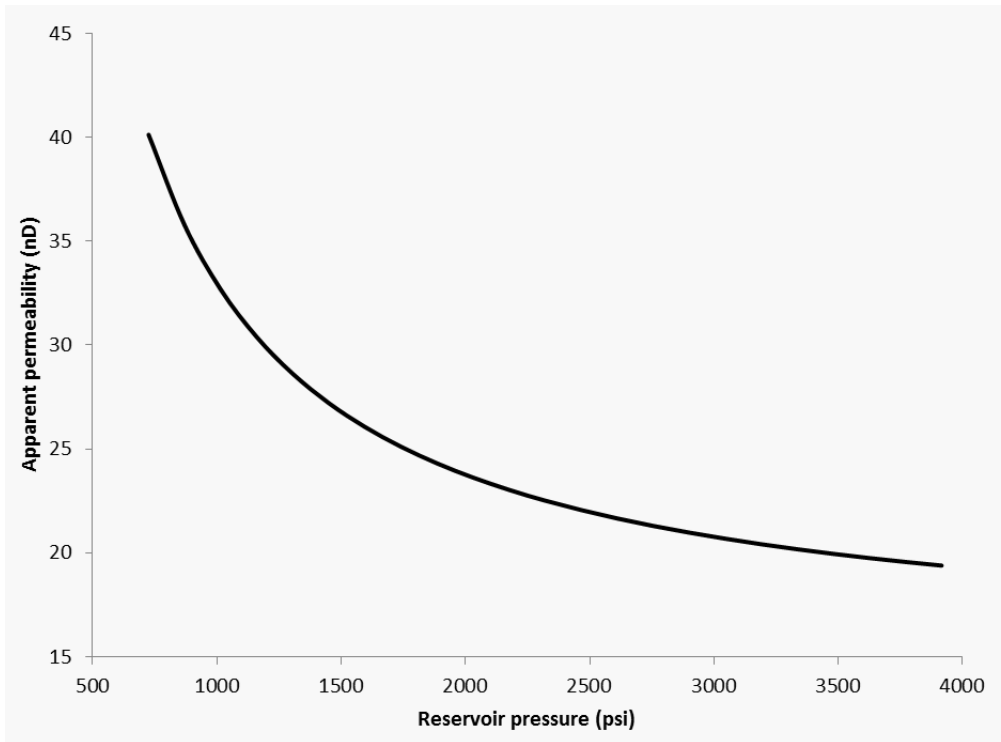
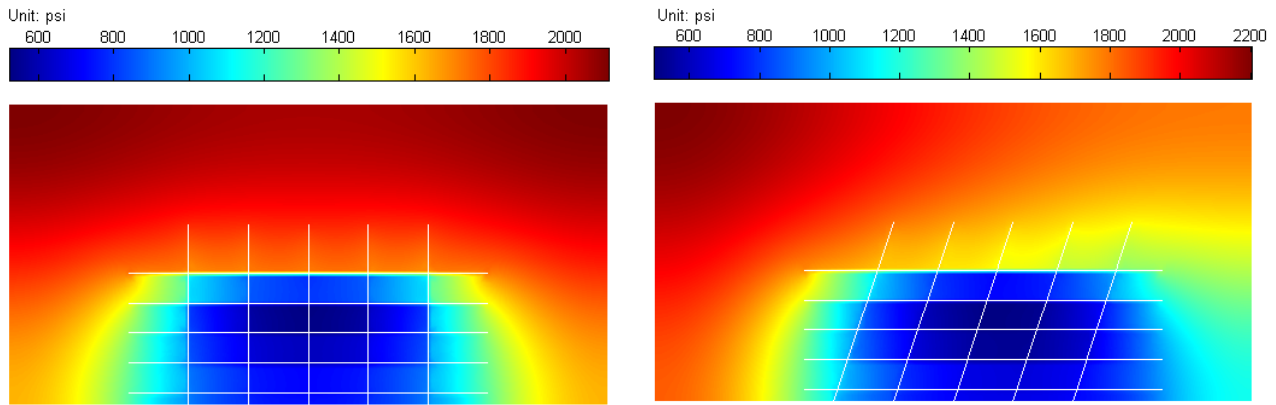


Figure 8: Pressure dependence of the apparent permeability under reservoir condition. With the decrease of pressure from 4000 psi to 700 psi, the apparent permeability has been more than doubled.



(a) Matrix pore pressure for orthogonal fractures after 3 years (b) Matrix pore pressure for oblique fractures after 3 years

Figure 9: Comparison for different fracture patterns with x-interval space 100m and y-interval space 50m. The white lines represent discrete fractures. The fracture connectivity determines pore pressure distribution. For orthogonal fracture network, the pressure field is symmetrical, but for oblique one, it is nonsymmetrical.

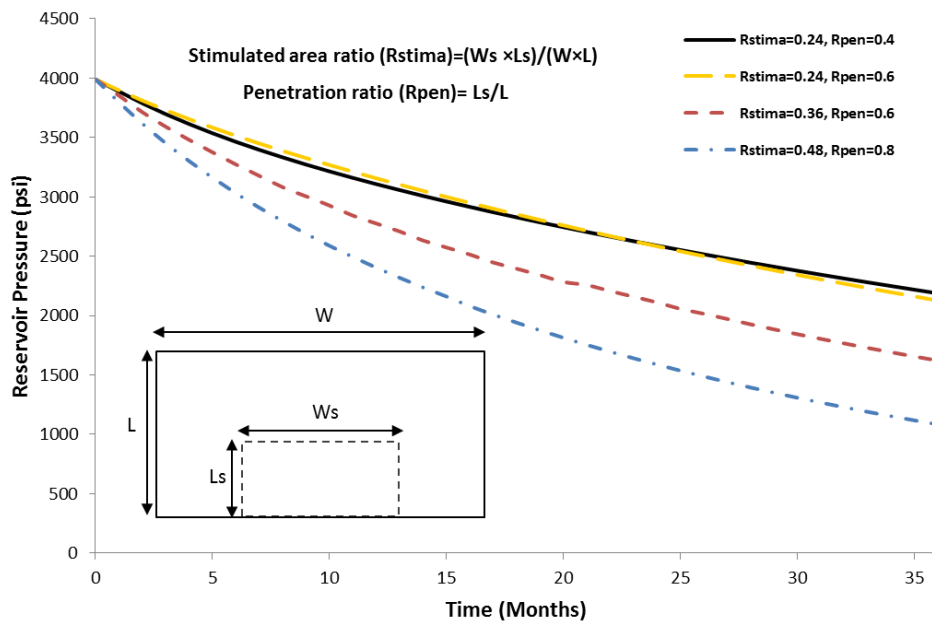


Figure 10: Comparison pressure declined lines for different stimulated area ratio and penetration ratios. It is found that the stimulated area is the main factor to effect drainage rate. The more stimulated area, the faster drainage rate is. For the same stimulated area, the pressure-declined curve is almost same, even though different penetration ratio.

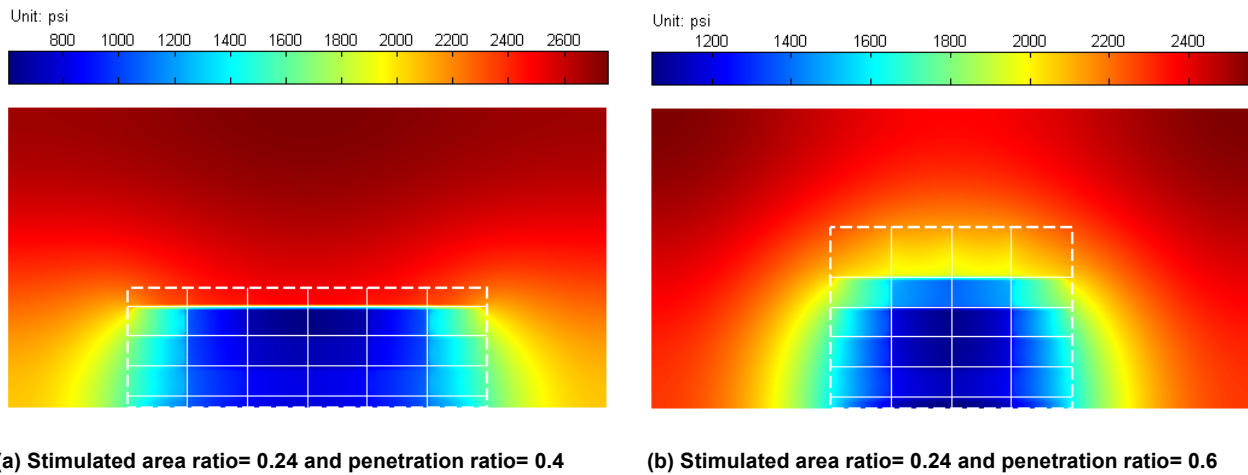


Figure 11: Comparison for different penetration ratio but with the same stimulated area ratio after 3 years. For the same stimulated area, the deeper fracture penetration can control the farther gas-in-place than shallower fracture penetration.

Table 1: Rock properties for Terzaghi problem

<i>Parameter</i>	<i>Symbol</i>	<i>Value</i>	<i>Unit</i>
Young modulus	E	80	GPa
Poisson's ratio	ν	0.30	No dimension
Matrix porosity	Φ_1	0.2	No dimension
Fracture porosity	Φ_2	0.05	No dimension
Fluid mobility in matrix	K_1/μ_1	1×10^{-6}	$\text{m}^2/(\text{mPa.s})$
Fluid mobility in fracture	K_2/μ_2	1×10^{-3}	$\text{m}^2/(\text{mPa.s})$

Table 2: The input parameters for the developed model, values of which are aligned with Barnett shale

<i>Parameter</i>	<i>Symbol</i>	<i>Value</i>	<i>Unit</i>
Initial reservoir pressure	P_0	4000	psi
Production pressure	P_w	500	psi
Horizontal maximum stress	σ_H	8700	psi
Horizontal minimum stress	σ_h	5800	psi
Young modulus	E	80	GPa
Poisson's ratio	ν	0.30	No dimension
Matrix porosity	Φ_1	0.05	No dimension
Fracture porosity	Φ_2	0.05	No dimension
Matrix intrinsic permeability	K_1	15	nD at the initial reservoir pressure
Fracture permeability	K_2	150	mD
Fracture width	w_f	10	mm